PHOTONICS Research

Actively logical modulation of MEMS-based terahertz metamaterial

Ruijia Xu, Xiaocan Xu, Bo-Ru Yang, Xuchun Gui, Zong Qin, and Yu-Sheng Lin*

School of Electronics and Information Technology, Sun Yat-sen University, Guangzhou 510006, China
**Corresponding author: linyoush@mail.sysu.edu.cn*

Received 26 January 2021; revised 12 April 2021; accepted 18 April 2021; posted 20 May 2021 (Doc. ID 420876); published 1 July 2021

The integration of micro-electro-mechanical system (MEMS) with metamaterial has provided a novel route to achieve programmability via its reconfigurable capabilities. Here, we propose and demonstrate a MEMS-based metadevice by using switchable winding-shaped cantilever metamaterial (WCM) for active logical modulation. WCM can be actuated by external driving voltage, and the logical modulation bit is performed by releasing MEMS cantilevers to represent "on" and "off" states. While the underneath substrate surface of a MEMS-based metadevice is rough after releasing the cantilevers, the metadevice is allowed to operate on the reconfigurable switching state and avoid the snapping down of the device when the system is overloaded. Such a reconfigurable and programmable MEMS-based metadevice exhibits multifunctional characteristics to simultaneously perform the logic operations of "OR" and "AND" gates. By exploiting the tuning mechanism of the MEMS-based metadevice, the arbitrary metamaterial configuration can be implanted into WCM. This opens a wide avenue to further enlarge the operating frequency range and applications in optoelectronic fields. These unique results provide various possibilities in multifunctional switching, active logical modulating, and optical computing applications.

https://doi.org/10.1364/PRJ.420876

1. INTRODUCTION

Metamaterials offer a strategy to artificially control electromagnetic waves on subwavelength scales and obtain unique optical response. Since the first experimental demonstration in 2000 [1], various metamaterial designs have attracted great interest due to their extraordinary properties, which cannot be found in traditional materials. Either the electric permittivity or magnetic permeability of metamaterials can be designed for desired application through the proper manipulation of the geometrical dimensions [2–6]. In general, they can be scaled to operate in the entire electromagnetic spectrum, including microwave [7], terahertz (THz) [8–12], infrared (IR) [13], and visible ranges [14]. With the rapid development of metamaterial, they have been reported in many fields, such as cloaking devices, thermophotovoltaics, microfluidic detection, and biomedical sensing [15–19].

Most current metamaterials can be passively controlled to perform a specific electromagnetic function. However, the active control for metamaterial designs has been desired to satisfy the requirements of real-world applications. As such, more and more researchers are paying attention to the active metamaterials via liquid crystal [20], laser pumping [21], phase transitions materials [22–24], and so on. However, many limitations exist among these tuning methods, owing to the nonlinear properties of natural materials. By artificially exploiting the electromagnetic force at the micro- and nanoscale, reconfigurable metamaterials are developed to achieve larger tuning range [25]. These reconfigurable metamaterials can be performed via the electromechanical method, i.e., micro-electro-mechanical systems (MEMS) technology [26–28]. MEMS-based metamaterials have been realized by using either an in-plane comb-drive actuator [29,30] or an out-of-plane bimorph actuator [31–33]. By using MEMS technology, the unit cell of metamaterial can be directly released and manipulated, which assists MEMS-based metamaterials to become candidates to help overcome the limitations of traditional tuning methods and provide an ideal platform for reconfigurable metamaterial.

For the reconfigurable capabilities of metamaterials, many researches have demonstrated the programmable metamaterial devices [34,35]. The optical programmable metamaterials are based on the electromagnetic switching response by using electromagnet [36], mechanical stretch [37], origami [38], and MEMS [39] methods, which have unlocked a new field for optical computing. However, most of these designs are only suitable for specific applications. To further increase the flexibility and applicability for the combo integration, the multifunctional characteristic is desired [40].

In this study, we numerically and experimentally demonstrate a design of reconfigurable metamaterial using a

MEMS-based cantilever array to make the incident THz wave tunable. The proposed reconfigurable metamaterial is composed of a winding-shaped cantilever metamaterial (WCM) fabricated on silicon (Si) substrate. Herein, the multilayer cantilevers are used as an electrothermal actuator (ETA) as well as resonator. The composition of ETA is photoresist (PR)/Au/Si_3N_4 from top to bottom. By applying a DC bias voltage, the released ETA could be actuated downward to the substrate. The mechanical, electrical, and optical properties of WCM are investigated to realize multifunctional devices. For the opto-logic application, the functions of "OR" and "AND" gates are simultaneously performed by using a MEMS-based WCM device. Meanwhile, the fabrication process of the MEMS-based WCM device provides an ideal platform to form tunable 3D metamaterial, which greatly improves the flexibility and applicability in metamaterial fields, such as multifunctional and logic computing applications.

2. DESIGN AND METHOD

Actuation of the proposed WCM devices is based on the thermal mismatch of different material components. Figure 1(a) shows schematic diagrams of a MEMS-based WCM device. The released ETA array is bent upward to realize the platform for various kinds of tunable 3D metamaterials. The geometrical denotations of the MEMS-based WCM device are indicated in Fig. 1(b). Herein, the corresponding parameters are $w_1 = 10\ \mu m$, $w_2 = 170\ \mu m$, $L = 450\ \mu m$, $P_x = 250\ \mu m$, and $P_y = 500\ \mu m$. All linewidths are kept as constant as 10 μm. The exposed transverse Si_3N_4 structure is designed to connect both sides of deformed ETAs. The working mechanism of ETA is induced by the mismatch of different thermal expansion coefficients within a multilayer cantilever, which causes the cantilever to bend upward through the fabrication process. By driving a DC bias voltage on the electrodes of ETAs, the resistance heat is induced by the current flow and then generated to provide the deformation of ETAs. The composition of ETAs is multilayer cantilever, which will be bent downward by increasing temperature and then realize the out-of-plane motion. ETAs work in the balanced state caused by the restoring force and the prestressing force. This behavior of ETAs is regarded as a reverse motion. A larger difference of thermal expansion coefficients generates a stronger driving force within the multilayer cantilever. To increase the height of the deformed ETA, a MEMS-based WCM device is designed to be composed of PR/Au/Si_3N_4 layers from top to bottom. The radius of curvature of the ETA can be expressed by the following equations [41]:

$$\frac{1}{R} = \frac{1}{C}\left[\Delta T(\alpha_1 - \alpha_2) - \left(\frac{1}{E_1} + \frac{1}{E_2}\right)\frac{2F_x(L-x)}{A(t_1+t_1)}\right], \quad (1)$$

$$C = 2\frac{E_1 I_1 + E_2 I_2}{A(t_1+t_1)}\left(\frac{1}{E_1} + \frac{1}{E_2}\right) + \frac{t_1+t_1}{2}, \quad (2)$$

$$F_x = \frac{\varepsilon_0 A}{2(h-x)^2}V^2, \quad (3)$$

$$h = 2R\sin^2(\theta/2), \quad (4)$$

where subscripts 1 and 2 represent different materials of two adjacent layers, respectively; ΔT is the temperature difference caused by the fabrication process; α is the thermal expansion coefficient; E is the Young's modulus; L is the length of the deformed cantilevers; x is the vertical displacement of the released cantilever with an applied DC bias voltage; A is the area of the curved beam; t is the thickness of deposited layer; I is the area moment of inertia; θ is the central angle; h is the height of the deformed cantilevers. Here, the thicknesses of PR/Au/Si_3N_4 layers are 1000, 100, and 500 nm, respectively.

3. RESULTS AND DISCUSSIONS

To further study the electrical and mechanical properties of a MEMS-based WCM device, the relationship between cantilever height and applied DC bias voltage is investigated. By applying a DC bias voltage, the released ETA can be bent downward to the Si substrate. The relationship of cantilever heights and the applied DC bias voltages is summarized in Fig. 2(a). The inserted optical images illustrate the bending deformations of a MEMS-based WCM device under different DC bias voltages. The initial state of the WCM device is bent upward and keeps unchanged until the applied DC bias voltage of 10 V. It can be clearly observed that the ETA is bent downward gradually and the cantilever height decreases by increasing the driving voltage to 20 V. The radius of curvature of the cantilever becomes smaller simultaneously, along with the cantilever bending downward. In the driving DC bias voltage

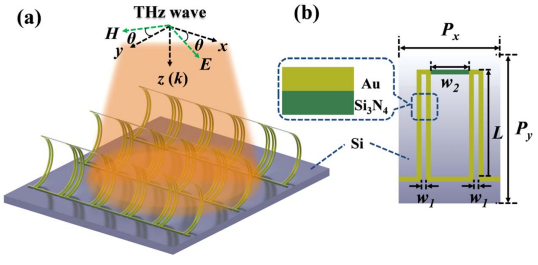

Fig. 1. Schematic drawings of (a) MEMS-based winding-shaped cantilever metamaterial (WCM) and (b) the geometrical denotations of the WCM unit cell.

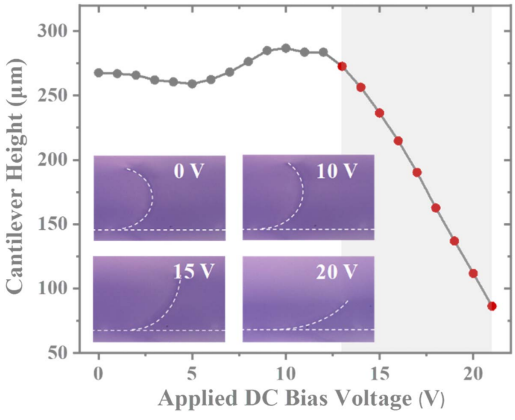

Fig. 2. Relationship of cantilever heights and the applied DC bias voltages. Inserted optical images illustrate the bending deformations of MEMS-based WCM device under different DC bias voltages.

from 0 to 12 V, the applied voltages do not reach the actuation point of ETA, and the ETA height keeps stable without moving downward. There is minor change caused from the measurement deviation. When the driving voltage reaches the actuation voltage of the ETA, the ETA begins to bend downward, and then the ETA height decreases. According to Eq. (3), the cantilever height is proportional to the driving voltage. A linear relationship of cantilever height and applied DC bias voltage is in the voltage range of 13 to 21 V, which is defined as the work region of a MEMS-based WCM device. The cantilever height decreases from 273 to 86 μm. The vertical moving distance is 187 μm. The cantilever always suffers the snapping down on the substrate when the driving voltage reaches the pull-in voltage, which is a drawback for most MEMS devices. Figures 3(a) and 3(b) show the SEM images of a MEMS-based WCM array and unit cell, respectively. The exposed Si substrate surface was patterned by using inductively coupled plasma etching isotopically, which makes the Si substrate surface textured roughly, as observed in the SEM image of Fig. 3(b). Therefore, the reconfigurable characteristic of a MEMS-based WCM device is realized as the side view of the SEM image, as shown in Fig. 3(c). The composition of the WCM device is PR/Au/Si_3N_4 from top to bottom, as illustrated in Fig. 3(d). The electrical and mechanical characteristics of the MEMS-based WCM device are stable and applicable.

The proposed tunable 3D metamaterial is formed through a MEMS process and can serve as a THz optical resonator. Such a design shows obvious asymmetric structure and exhibits polarization-dependent characteristics. Figures 4(a) and 4(b) show the simulated and measured transmission spectra of a MEMS-based WCM device without driving DC bias voltage, respectively. The polarization angle is defined as the intersection angle between the *E*-field and *x* axis direction, as indicated in Fig. 1(a). By increasing the polarization angle, the resonant intensity at 0.33 THz decreases gradually from 86% to 22%. The tuning range of resonant intensity is 64%. In Fig. 4(b), the measured resonant intensity at 0.33 THz decreases gradually from 88% to 30% by increasing the polarization angle. The tuning range of resonant intensity is 58%, and the resonance keeps at 0.33 THz. These measurement results are in agreement compared with the simulation results. These results provide a design solution for the THz variable optical attenuator (VOA) application by changing the polarization angle.

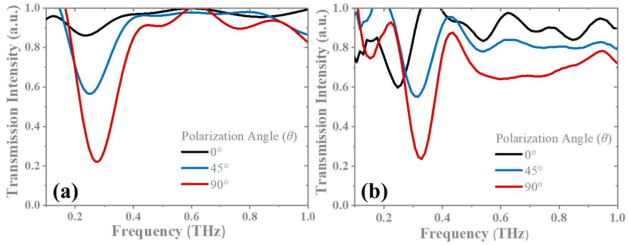

Fig. 4. (a) Simulated and (b) measured transmission spectra of MEMS-based WCM device without driving voltages at different incident polarization angles.

Since the optical properties of metamaterial are determined via manipulation of the geometrical dimensions, the transmission spectra of the proposed WCM devices can be tuned by exploiting the deformation of ETAs. The simulated and measured results for the influences of driving different DC bias voltages on the transmission spectra of MEMS-based WCM device are summarized in Fig. 5. At the condition of $\theta = 0°$, the relationships of simulated and measured transmission spectra of MEMS-based WCM devices with different driving voltages are shown in Figs. 5(a) and 5(d), respectively. By driving a DC bias voltage of 20 V, the resonances are blue-shifted less than 0.03 THz, which can be regarded as unchanged at 0.33 THz, owing to the deviation of simulation and measurement results. The resonant intensity decreases from 86% to 80%. In Fig. 5(b), the resonant intensity decreases to 56% at 0.33 THz by increasing the polarization angle to 45°. By driving the DC bias voltage from 11 to 20 V, the resonant intensity decreases gradually to 49%. At the condition of $\theta = 90°$, the resonant intensity decreases from 22% to 11% by driving a DC bias voltage from 11 to 20 V, as shown in Fig. 5(c). The characteristic of controllable resonant intensity can be clearly observed in the simulated results. The measured results for the MEMS-based WCM device operated at $\theta = 0°$, 45°, and 90° driving different voltages are summarized in Figs. 5(d)–5(f), respectively. The resonances are kept stable, and the resonant intensities are also kept stable at 88%, as shown in Fig. 5(d). By increasing the polarization angle to

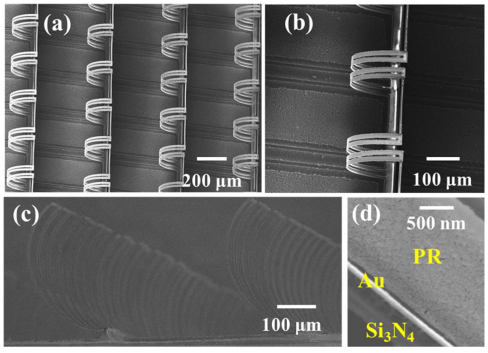

Fig. 3. SEM images of MEMS-based WCM device. Top views of MEMS-based WCM (a) array and (b) unit cell. (c) Side view of MEMS-based WCM device. (d) Composition of WCM single-cantilever.

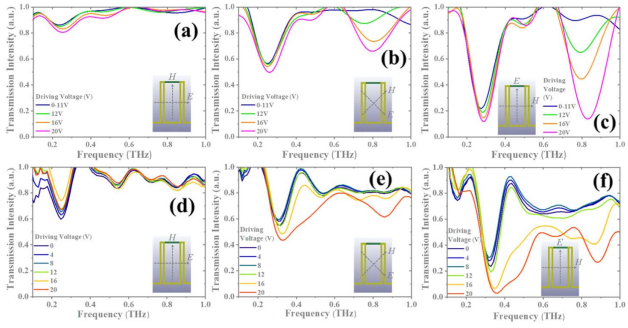

Fig. 5. (a)–(c) Simulated and (d)–(f) measured transmission spectra of MEMS-based WCM device at different driving voltages for polarization angles of (a), (d) $\theta = 0°$; (b), (e) $\theta = 45°$; and (c), (f) $\theta = 90°$, respectively.

45°, the resonant intensity decreases from 53% to 43% at 0.33 THz by driving a DC bias voltage from 11 to 20 V, as shown in Fig. 5(e). At the condition of $\theta = 90°$, the resonant intensity decreases from 30% to 7% at 0.33 THz by driving a DC bias voltage from 11 to 20 V, as shown in Fig. 5(f). The intensity of the second resonance decreases from 72% to 27% at 0.88 THz by driving a DC bias voltage from 11 to 20 V. These above-mentioned electromagnetic characteristics of the MEMS-based WCM device can be precisely tuned by changing polarization angles and driving different DC bias voltages. It proves that a MEMS-based WCM device is quite suitable for the use in the VOA and switch applications.

The optical switching performance is a key parameter for the THz switching function. To evaluate the optical switching performance of the MEMS-based WCM device, the switching ratio is defined as the resonant intensity at the condition of $\theta = 0°$ without driving voltage divided by the measured resonant intensity at the conditions of $\theta = 0°$, 45°, and 90° with different driving voltages. The optical switching performances of the MEMS-based WCM device are calculated and summarized in Fig. 6. In Fig. 6(a), the optical switching ratio increases from 1.0 to 3.0 by increasing the polarization angle from 0° to 90° operated at 0.33 THz and without driving voltage. The initial tuning range of the optical switching ratio is 3.0. By driving DC bias voltage from 0 to 20 V, the optical switching ratio is increased from 3.0 to 4.2 when changing the polarization angle from $\theta = 0°$ to $\theta = 90°$. In Fig. 6(b), the optical switching ratios for a device operating at 0.88 THz are kept as stable by changing the polarization angle from $\theta = 0°$ to $\theta = 90°$ and driving voltage within 12 V. When the driving voltage is over 12 V, the optical switching ratio is increased to 3.2 for the polarization angle $\theta = 90°$. It can be enhanced by increasing the polarization angle and driving voltage. The best optical switching performance is exhibited by a MEMS-based WCM device operated at the polarization angle $\theta = 90°$ and driving voltage of 20 V.

The MEMS-based WCM device shows obvious dual-resonance and polarization-dependent characteristics. These characteristics can be expressed as optical signals for "on" and "off" states, which can be used in the opto-logic operation application. Such varied transmission signals need to be received by an integrated detector. To detect the modulated optical signals from a MEMS-based WCM device, a programmable device is proposed with an integration of the MEMS-based WCM device and metamaterial perfect absorber (MPA), as illustrated

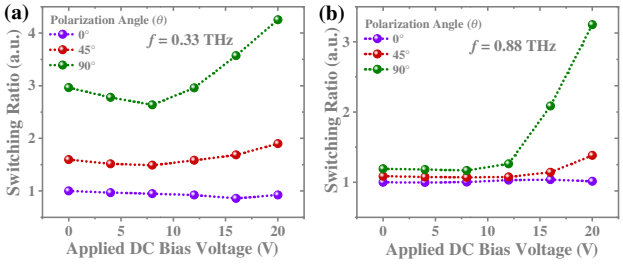

Fig. 6. Optical switching performances of MEMS-based WCM device operating at different driving voltages and monitoring at (a) 0.33 THz and (b) 0.88 THz.

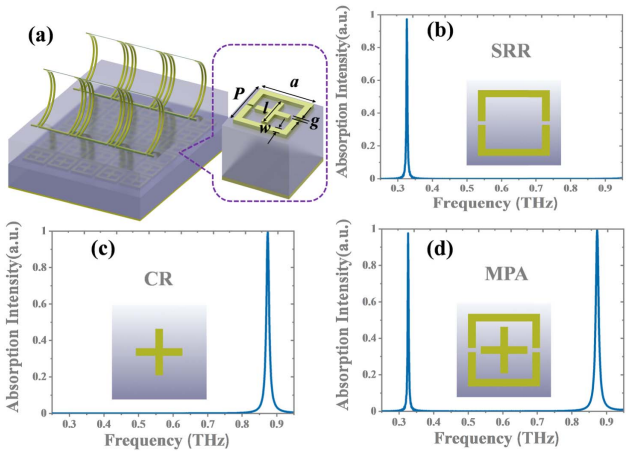

Fig. 7. (a) Schematic drawings of MEMS-based WCM device integrated with MPA. Absorption spectra of (b) SRR, (c) CR, and (d) MPA. Insert images are drawings of unit cells. The geometrical dimensions are defined as $l = 85$ μm, $w = 15$ μm, $a = 135$ μm, $g = 5$ μm, and $P = 155$ μm.

in Fig. 7(a). The MPA is fabricated by using a superposition of a split-ring resonator (SRR) and cross-shaped resonator (CR) on an Au mirror layer sandwiched by a dielectric spacer. For MPA, the absorption (A) is defined as $A = 1 - R - T$, where R and T are the reflection and transmission of the MPA. Owing to the transmission of the MPA being inhibited by the bottom Au mirror layer, A can be expressed by $A = 1 - R$. The MPA is designed to realize perfect absorption at 0.33 and 0.88 THz generated from the configuration of SRR and CR structures. Figures 7(b) and 7(c) show the absorption spectra of SRR and CR with the same periods, respectively. SRR exhibits perfect absorption at 0.33 THz, while CR exhibits perfect absorption at 0.88 THz. By superimposing SRR and CR together, there is a dual-resonance characteristic at 0.33 and 0.88 THz, as shown in Fig. 7(d). Such an MPA is deigned to perform the detection of resonances generated from a MEMS-based WCM device.

The optical detection performances of the programmable device integrated with the MEMS-based WCM device and MPA at 0.33 and 0.88 THz are further discussed. Figure 8(a) shows the absorption efficiency (AE) of the programmable device for the polarization angle $\theta = 0°$. The efficiencies are stable owing to the driving voltage insensitive to resonance at the condition of polarization angle $\theta = 0°$, as shown in Fig. 5(d). By increasing the polarization angle to $\theta = 45°$, the absorption efficiencies are 0.56 at 0.33 THz and 0.79 at 0.88 THz without driving voltage. When the driving voltage increases to 20 V, the absorption efficiencies decrease to 0.43 at 0.33 THz and 0.69 at 0.88 THz. Similarly, the resonances decrease at 0.33 and 0.88 THz by driving voltage of 20 V under the condition of $\theta = 90°$. The modulated logic signals could be clearly distinguished and detected by driving a DC bias voltage of 20 V and changing the polarization angle.

By exploiting the optical performance of WCM devices at 0.33 and 0.88 THz, the logic operations of "OR" and "AND" gates can be simultaneously performed. Figure 9 summarizes

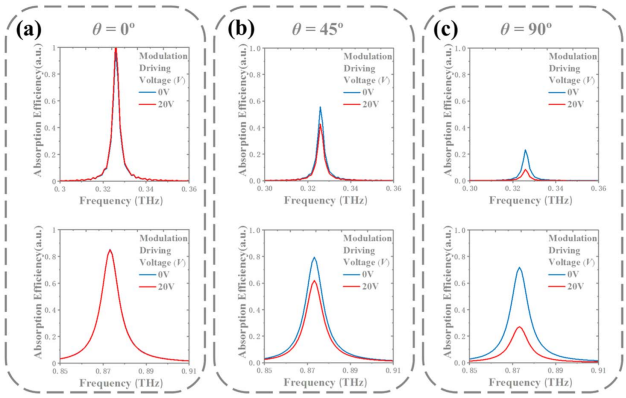

Fig. 8. AE of programmable device for the polarization angle of (a) $\theta = 0°$, (b) $\theta = 45°$, and (c) $\theta = 90°$, respectively.

the logic functions of the proposed programmable device integrated with a MEMS-based WCM device and MPA. The logical operation function of the "OR" gate is realized at 0.33 THz, as shown in Fig. 9(a). Two external input signals are the incident polarization angle and driving DC bias voltage. Herein, the input conditions of polarization angles for $\theta = 45°$ and $\theta = 90°$ are defined as logic signal "0" and "1," respectively. Meanwhile, the input conditions of driving voltages for $V = 0$ V and $V = 20$ V are defined as logic signal "0" and "1," respectively. The output signal is dependent on the detected AE, which equals 0.5 defined as a threshold condition. When AE is less than 0.5, WCM represents the logic signal "on" state, i.e., logic signal "1." When AE is greater than 0.5, WCM represents the logic signal "off" state, i.e., logic signal "0." As shown in Fig. 9(a), the output signal is "0" for AE being 0.56 at 0.33 THz under the condition of polarization angle of 45° ("0") and without driving voltage ("0"), while the output signal is "1" for AE being 0.43 at 0.33 THz under the condition of a 45° polarization angle ("0") and with a driving voltage of 20 V ("1"). By increasing the polarization angle to 90°, AE values are less than 0.5 without and with a driving voltage, which always represents the logic signal "1" state. Thus, the corresponding relationships between the inputs and outputs can be defined as logic "OR" gate function. Figure 9(b) shows the programmable device exhibits logic "AND" gate function at 0.88 THz. AE values are greater than 0.5 for the programmable device without and with driving voltage at the condition of polarization angle $\theta = 45°$. The output signals are "0" states. When the incident polarization angle is 90°, the AE value of the programmable device at 0.88 THz decreases from 0.72 to 0.27 by increasing the driving voltage from 0 to 20 V. The output signals are "0" and "1" states, respectively. The optical responses of the programmable device operated at 0.88 THz can be defined as the logic "AND" gate function. The logic "OR" and "AND" gates are the basic and key components in the opto-logic operation device. The proposed programmable device exhibits the opto-logic operation function of "OR" and "AND" gates simultaneously. It provides the possibilities for the applications of programmable optical devices, optics digital processors, and modulators in the THz frequency range.

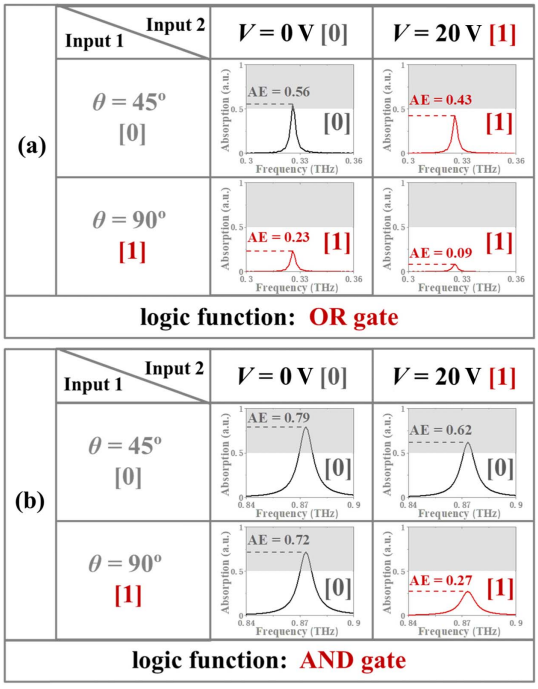

Fig. 9. Programmable device is functionalized as logic (a) OR and (b) AND gates. They are working at the frequency of 0.33 THz and 0.88 THz, respectively.

The large tuning range of resonance is a key factor for logical modulation of a THz device. The proposed MEMS-based WCM device provides an ideal platform to implant various kinds of metamaterial configurations on the central area of a WCM platform. Herein, a typical metamaterial configuration, i.e., electric spilt-ring resonator (eSRR) is chosen to be integrated into the MEMS-based WCM device as the SEM image shows in Fig. 10(a). The eSRR pattern is fabricated on the dielectric Si_3N_4 layer, which is used as the connection between a winding-shaped cantilever and eSRR. The eSRR-WCM device is bent upward uniformly after releasing the structures as the SEM image of eSRR-WCM array shown in Fig. 10(b). In Fig. 10(c), it can be clearly observed that the eSRR-WCM device exhibits a dual-band characteristic in the range from 0.1 to

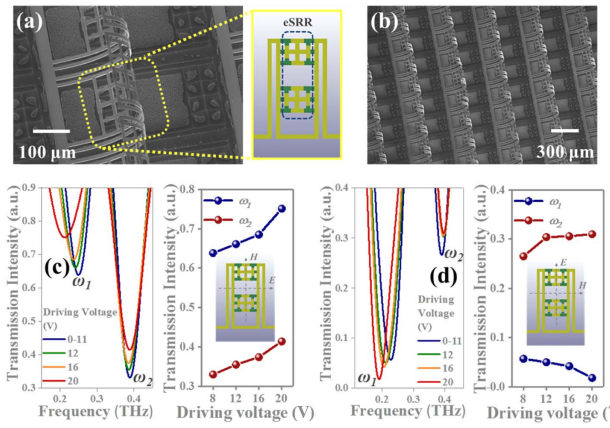

Fig. 10. SEM images of eSRR-WCM (a) unit cell and (b) array. (c) The measured transmission spectra of eSRR-WCM at (c) $\theta = 0°$ and (d) $\theta = 90°$ by driving different voltages.

0.5 THz. It means that the eSRR pattern can be integrated on the WCM platform and generates an extra resonance compared with that without an eSRR pattern at the condition of $\theta = 0°$. By increasing the driving voltage from 0 to 20 V, the resonant intensity at 0.39 THz increases from 33% to 41%. When the polarization angle increases to 90°, the resonances of the eSRR-WCM device are enhanced around 0.20 THz and weakened around 0.40 THz by driving different voltages, as shown in Fig. 10(d). These results show that the integration of a MEMS-based WCM device and arbitrary metamaterial configuration has the potential to achieve single-, dual-, and multi-resonance for widespread optoelectronic applications.

4. CONCLUSION

In conclusion, a MEMS-based WCM device is demonstrated to realize a high-efficient optical switch, VOA, and programmable device. By driving an external voltage, the released cantilevers will be bent downward to the Si substrate surface. The resonant intensity at 0.33 THz decreases from 71% to 22% by changing the polarization angle from 0° to 90°. Moreover, the resonant intensity could be tuned by driving different bias voltage to perform the optical switch and VOA applications. The combination of changing polarization angle and driving bias voltage realizes the MEMS-based WCM device to exhibit the programmable characteristic. The MEMS-based WCM device shows better optical switching performance under the condition of polarization angle $\theta = 90°$ and driving bias voltage of 20 V. The maximum switching ratio is 3.2. In the programmable modulation, the logic operation function of the "OR" gate is realized for the MEMS-based WCM device operated at 0.33 THz, and that of the "AND" gate is realized for the MEMS-based WCM device operated at 0.88 THz. Such a MEMS-based WCM device provides an ideal 3D platform to serve as a designed arbitrary metamaterial configuration implanted into the central area of the MEMS-based WCM device for widespread applications, such as multifunctional switches and programmable modulators.

Funding. Natural Science Foundation of Basic and Applied Foundation of Guangdong Province (2021A1515012217); National Key Research and Development Program of China (2019YFA0705004); National Natural Science Foundation of China (11690031).

Acknowledgment. The authors acknowledge the State Key Laboratory of Optoelectronic Materials and Technologies of Sun Yat-sen University for the use of experimental equipment.

Disclosures. The authors declare no conflicts of interest.

REFERENCES

1. J. B. Pendry, "Negative refraction makes a perfect lens," Phys. Rev. Lett. **85**, 3966–3969 (2000).
2. D. R. Smith, J. B. Pendry, and M. C. K. Wiltshire, "Metamaterials and negative refractive index," Science **305**, 788–792 (2004).
3. C. M. Watts, X. L. Liu, and W. J. Padilla, "Metamaterial electromagnetic wave absorbers," Adv. Mater. **24**, OP98–OP120 (2012).
4. Y. X. Cui, K. H. Fung, J. Xu, H. J. Ma, Y. Jin, S. L. He, and N. X. Fang, "Ultrabroadband light absorption by a sawtooth anisotropic metamaterial slab," Nano Lett. **12**, 1443–1447 (2012).
5. M. M. Hossain, B. H. Jia, and M. Gu, "A metamaterial emitter for highly efficient radiative cooling," Adv. Opt. Mater. **3**, 1047–1051 (2015).
6. W. Li, U. Guler, N. Kinsey, G. V. Naik, A. Boltasseva, J. G. Guan, V. M. Shalaev, and A. V. Kildishev, "Refractory plasmonics with titanium nitride: broadband metamaterial absorber," Adv. Mater. **26**, 7959–7965 (2014).
7. D. Schurig, J. J. Mock, B. J. Justice, S. A. Cummer, J. B. Pendry, A. F. Starr, and D. R. Smith, "Metamaterial electromagnetic cloak at microwave frequencies," Science **314**, 977–980 (2006).
8. H. T. Chen, W. J. Padilla, J. M. O. Zide, A. C. Gossard, A. J. Taylor, and R. D. Averitt, "Active terahertz metamaterial devices," Nature **444**, 597–600 (2006).
9. X. Xu, R. Xu, and Y.-S. Lin, "Tunable terahertz double split-ring metamaterial with polarization-sensitive characteristic," Opt. Laser Technol. **141**, 107103 (2021).
10. Y. Wen, K. Chen, and Y.-S. Lin, "Terahertz metamaterial resonator with tunable Fano-resonance characteristic," Results Phys. **23**, 104049 (2021).
11. F. Lu, H. Ou, and Y.-S. Lin, "Reconfigurable terahertz switch using flexible L-shaped metamaterial," Opt. Lett. **45**, 6482–6485 (2020).
12. W. Yang and Y.-S. Lin, "Tunable metamaterial filter for optical communication in the terahertz frequency range," Opt. Express **28**, 17620–17629 (2020).
13. Y. Zhang, P. Lin, and Y.-S. Lin, "Tunable split-disk metamaterial absorber for sensing application," Nanomaterials **11**, 598 (2021).
14. Y.-S. Lin, J. Dai, Z. Zeng, and B.-R. Yang, "Metasurface color filters using aluminum and lithium niobate configurations," Nanoscale Res. Lett. **15**, 77 (2020).
15. Y.-S. Lin and Z. Xu, "Reconfigurable metamaterials for optoelectronic applications," Int. J. Optomechatron. **14**, 78–93 (2020).
16. D. Zheng and Y.-S. Lin, "Tunable dual-split-disk resonator with electromagnetically induced transparency characteristic," Adv. Mater. Technol. **5**, 2000584 (2020).
17. X. J. Ni, Z. J. Wong, M. Mrejen, Y. Wang, and X. Zhang, "An ultrathin invisibility skin cloak for visible light," Science **349**, 1310–1314 (2015).
18. H. Ou, F. Lu, Z. Xu, and Y.-S. Lin, "Terahertz metamaterial with multiple resonances for biosensing application," Nanomaterials **10**, 1038 (2020).
19. R. Xu and Y.-S. Lin, "Tunable infrared metamaterial emitter for gas sensing application," Nanomaterials **10**, 1442 (2020).
20. D. Shrekenhamer, W. C. Chen, and W. J. Padilla, "Liquid crystal tunable metamaterial absorber," Phys. Rev. Lett. **110**, 177403 (2013).
21. M. Gupta, Y. K. Srivastava, and R. Singh, "A toroidal metamaterial switch," Adv. Mater. **30**, 1704845 (2018).
22. R. N. Dao, X. R. Kong, H. F. Zhang, and X. L. Tian, "A tunable ultrabroadband metamaterial absorber with multilayered structure," Plasmonics **15**, 169–175 (2020).
23. K. Appavoo and R. F. Haglund, "Detecting nanoscale size dependence in VO_2 phase transition using a split-ring resonator metamaterial," Nano Lett. **11**, 1025–1031 (2011).
24. H. Wang, Y. Yang, and L. P. Wang, "Switchable wavelength-selective and diffuse metamaterial absorber/emitter with a phase transition spacer layer," Appl. Phys. Lett. **105**, 071907 (2014).
25. J. Y. Ou, E. Plum, J. F. Zhang, and N. I. Zheludev, "Giant nonlinearity of an optically reconfigurable plasmonic metamaterial," Adv. Mater. **28**, 729–733 (2016).
26. X. Hu and Y.-S. Lin, "Programmable terahertz metamaterial with multiple logic characteristics," Results Phys. **18**, 103267 (2020).
27. Y. Han, J. Lin, and Y.-S. Lin, "Tunable metamaterial-based silicon waveguide," Opt. Lett. **45**, 6619–6622 (2020).
28. Z. Xu and Y.-S. Lin, "A stretchable terahertz parabolic-shaped metamaterial," Adv. Opt. Mater. **7**, 1900379 (2019).
29. T. Xu, X. Xu, and Y.-S. Lin, "Tunable terahertz free spectra range using electric split-ring metamaterial," J. Microelectromech. Syst. **30**, 309–314 (2021).
30. T. Xu, R. Xu, and Y.-S. Lin, "Tunable terahertz metamaterial using electrostatically electric split-ring resonator," Results Phys. **19**, 103638 (2020).

31. R. Xu and Y.-S. Lin, "Reconfigurable multiband terahertz metamaterial using triple-cantilevers resonator array," J. Microelectromech. Syst. **29**, 1167–1172 (2020).
32. F. Zhan and Y.-S. Lin, "Tunable multiresonance using complementary circular metamaterial," Opt. Lett. **45**, 3633–3636 (2020).
33. R. Xu and Y.-S. Lin, "Flexible and controllable metadevice using self-assembly MEMS actuator," Nano Lett. **21**, 3205–3210 (2021).
34. Z. Xu, Z. Lin, S. Cheng, and Y.-S. Lin, "Reconfigurable and tunable terahertz wrench-shape metamaterial performing programmable characteristic," Opt. Lett. **44**, 3944–3947 (2019).
35. Y. Liao and Y.-S. Lin, "Reconfigurable terahertz metamaterial using split-ring meta-atoms with multifunctional electromagnetic characteristics," Appl. Sci. **10**, 5267 (2020).
36. Z. W. Wang, Q. Zhang, K. Zhang, and G. K. Hu, "Tunable digital metamaterial for broadband vibration isolation at low frequency," Adv. Mater. **28**, 9857–9861 (2016).
37. K. J. Fu, Z. H. Zhao, and L. H. Jin, "Programmable granular metamaterials for reusable energy absorption," Adv. Funct. Mater. **29**, 1901258 (2019).
38. H. B. Fang, S. C. A. Chu, Y. T. Xia, and K. W. Wang, "Programmable self-locking origami mechanical metamaterials," Adv. Mater. **30**, 1706311 (2018).
39. F. Zhu and Y.-S. Lin, "Programmable multidigit metamaterial using terahertz electric spilt-ring resonator," Opt. Laser Technol. **134**, 106635 (2021).
40. D. H. Le and S. Lim, "Four-mode programmable metamaterial using ternary foldable origami," ACS Appl. Mater. Interfaces **11**, 28554–28561 (2019).
41. M. Shavezipur, W. J. Gou, C. Carraro, and R. Maboudian, "Characterization of adhesion force in MEMS at high temperature using thermally actuated microstructures," J. Microelectromech. Syst. **21**, 541–548 (2012).